UC Davis
UC Davis Previously Published Works

Title
Large-Eddy Simulations of turbulent flow through a heated square duct

Permalink
https://escholarship.org/uc/item/9sp7b7h5

Authors
Schindler, A
Younis, BA
Weigand, B

Publication Date
2019

DOI
10.1016/j.ijthermalsci.2018.09.018

Peer reviewed

eScholarship.org Powered by the California Digital Library
University of California

International Journal of Thermal Sciences 135 (2019) 302–318

Contents lists available at ScienceDirect

International Journal of Thermal Sciences

journal homepage: www.elsevier.com/locate/ijts

Large-Eddy Simulations of turbulent flow through a heated square duct

A. Schindler[a], B.A. Younis[b,*], B. Weigand[a]

[a] Institut für Thermodynamik der Luft- und Raumfahrt, Universität Stuttgart, Stuttgart, Germany
[b] Department of Civil & Environmental Engineering, University of California, Davis, USA

ARTICLE INFO

Keywords:
LES
Square duct
Heat transfer
Thermal log-law
High-efficiency cooling systems

ABSTRACT

The behavior of the flow through a straight square duct is examined using Large-Eddy Simulations. Both isothermal and non-isothermal conditions were considered, the latter generated with either the wall temperature or the wall heat flux held constant. Fully-developed conditions were attained by initializing the velocity field with perturbed streamwise streaks, and by employing a method for efficiently applying cyclic boundary conditions to the velocity field while minimizing aliasing errors. Results were obtained for two values of bulk Reynolds numbers, Re_b = 6,000 and 10,000. The numerical accuracy was checked via several alternative methods that included performing computations on grids with different resolutions, both with and without sub-grid scale models. The results were used to test some of the assumption underlying the use of RANS approaches to predict the flow and thermal fields. Of particular interest was the examination of the effects of the turbulence-driven secondary motions on the near-wall processes, especially on existence and extent of the thermal logarithmic law of the wall, and on departures from the Reynolds analogy. Their effect on the turbulent Prandtl number was quantified, and the implications on the use of Fourier's law to relate the turbulent heat fluxes to the gradients on mean temperature are discussed.

1. Introduction

The turbulent flow of a fluid in a square duct is of practical interest for its frequent occurrence in engineering practice such as in high performance heat exchangers and in the cooling passages in gas-turbine blades [1]. It is also of fundamental interest due to the presence of turbulence-driven secondary flows that impact the rates of transfer of heat and momentum leading to distortion of the mean flow field, and to non-uniform distributions of shear stresses and heat fluxes on the duct walls. The prediction of these flows has exposed the limitations of many of the most-widely used RANS approaches for the prediction of turbulent flows. These approaches, being based on Boussinesq's assumption of linear stress-strain relationship, predict, in fully-developed flow conditions, isotropy of the normal stresses. Since it is the anisotropy of these stresses that provides the sole mechanism for generating the secondary flows, these are not obtained leading to significant errors in the prediction of important parameters such as the pressure drop and the overall heat-transfer rate [2]. Models that are based on non-linear stress-strain relationships (e.g. Refs. [3] [4]), or that involve the solution of modeled differential transport equations for all six non-zero components of the Reynolds-stress tensor ([5]) are more successful in capturing the details of the secondary flows but uncertainties remain, especially in predicting the consequences of these motions on the thermal field.

In contrast to conventional turbulence closures, the use of Large-Eddy Simulations (LES) to predict the behavior of turbulent flows involves fewer modeling assumptions and can thus potentially provide more reliable means for engineering predictions. Several studies of flows in square ducts with LES have been reported in the literature. For isothermal flows, these include the studies of Madabhushi and Vanka [6] and Breuer and Rodi [7]. For non-isothermal flows, results have been reported by Pallares and Davidson [8], Vázquez and Métais [9], Qin and Pletcher [10] and Zhu et al. [11]. Recently, Direct Numerical Simulations (DNS) have been used to study the fundamental flow physics associated with turbulence-driven secondary motions in ducts of increasing aspect ratio ([12]). The computations, which were performed using a Spectral-Element Method with a number of nodes of up to 326×10^6, revealed a degree of complexity arising from the interaction of bursting mechanisms from horizontal and vertical walls that would be hard to capture with either LES or RANS. Within the constraints of computational resources, the LES approach will probably remain the advanced design tool of choice for the foreseeable future.

In this paper, we make comparisons with some of the previously-reported LES results and proceed further in investigating in far more

* Corresponding author.
E-mail address: bayounis@ucdavis.edu (B.A. Younis).

https://doi.org/10.1016/j.ijthermalsci.2018.09.018
Received 15 May 2018; Received in revised form 10 September 2018; Accepted 11 September 2018
Available online 28 September 2018
1290-0729/ © 2018 Elsevier Masson SAS. All rights reserved.

detail the sensitivity of the predictions to some of the assumptions and practices underlying the use of LES in the prediction of heat transfer in square ducts. Amongst the issues examined is the intersection between grid resolution and the models used to approximate the sub-grid scale fluxes of momentum and thermal energy. We also examine the efficacy of methods used to generate initial conditions that lead to the rapid establishment of a sustainable turbulence field, and of methods for incorporating cyclic boundary conditions that minimize aliasing errors. Thus one objective of this research was to contribute a reliable set of results to the rather limited literature related to the use of LES in the prediction of non-isothermal flows in non-circular ducts. Another objective stems from the recognition that the task of obtaining numerically-accurate LES results within reasonable turn-around times is not trivial and in many cases precludes the use of this methodology for routine engineering design. There is thus some benefit in using LES to obtain descriptions of the flow details that are difficult to obtain via measurements, and to use these to examine some of the assumptions underlying the more practical RANS approaches. Amongst these is the assumption of the existence of logarithmic laws of the wall for momentum and temperature to obtain wall boundary conditions for these parameters (the 'wall functions' approach), and the assumption that the Reynolds analogy connecting the rates of heat and momentum transport via a constant Prandtl number holds even in the presence of anisotropy-driven secondary motions. We use our results to test both of these assumptions.

2. Mathematical formulation and computational details

The methodology underlying the Large-Eddy Simulations approach to modeling turbulent flows is well know (see, for example [13,14]). Briefly, the instantaneous equations governing the conservation of mass, momentum and energy are filtered to yield:

$$\frac{\partial \overline{U_i}}{\partial x_i} = 0 \tag{1}$$

$$\frac{\partial \overline{U_i}}{\partial t} + \frac{\partial}{\partial x_j}(\overline{U_i}\,\overline{U_j}) = -\frac{1}{\rho}\frac{\partial \overline{p}}{\partial x_i} + \frac{\partial}{\partial x_j}\left(\nu\frac{\partial U_i}{\partial x_j}\right) - \frac{\partial \tau_{ij}}{\partial x_i} \tag{2}$$

$$\frac{\partial \overline{\Theta}}{\partial t} + \frac{\partial(\overline{U_j}\,\overline{\Theta})}{\partial x_j} = \frac{\partial}{\partial x_j}\left(\Gamma\frac{\partial \overline{\Theta}}{\partial x_j}\right) - \frac{\partial \tau_{\Theta j}}{\partial x_j} \tag{3}$$

We use the Smagorinsky [15] model for the sub-grid scale stresses:

$$\tau_{ij} = -\nu_{sgs} 2\overline{S}_{ij} \tag{4}$$

where ν_{sgs} is the turbulent eddy viscosity and $\overline{S}_{ij}$ is the resolved strain rate tensor. The turbulent eddy viscosity is obtained from

$$\nu_{sgs} = (C_S\Delta)^2|\overline{\boldsymbol{S}}| \tag{5}$$

where Δ is a length scale obtained from

$$\Delta = (\Delta_x\Delta_y\Delta_z)^{\frac{1}{3}} \tag{6}$$

is used, where Δ_x, Δ_y, Δ_z is the grid spacing in x, y, z, respectively.

Several different values for the Smagorinsky constant C_S have previously been used in this and similar flows. In this work, C_S was set equal to 0.065 which is in line with the recommendations of [16,17] for wall-bounded flows.

The Smagorinsky model with a constant C_S tends to overpredict the viscosity in close proximity to the wall [18]. Following the usual practice, we use van Driest's damping function to bring about the correct behavior:

$$\nu_{sgs} = (C_S\Delta)^2|\overline{\boldsymbol{S}}|\left(1 - e^{-y^+/A^+}\right) \tag{7}$$

where $y^+ = \frac{u_\tau y}{\nu}$ is the non-dimensional wall distance and $A^+ = 26$.

The unresolved heat fluxes are modeled according to [13,17,19] as

$$\tau_{\Theta j} = -\Gamma_{sgs}\frac{\partial \Theta}{\partial x_j} \tag{8}$$

where

$$\Gamma_{sgs} = \frac{\nu_{sgs}}{\mathrm{Pr}_{sgs}} \tag{9}$$

is the thermal sub-grid scale diffusivity, ν_{sgs} is the sub-grid scale eddy viscosity in Eq. (7) and Pr_{sgs} is the sub-grid scale Prandtl number which was set equal to 0.4 in line with the recommendations of [19,20].

The simulations were performed using the open source CFD software OpenFOAM. Fluid properties for dry air at 293.15 K were assumed to be constant for both isothermal and heated flow conditions thus the temperature variations did not influence the flow field. Turning to details of the discretization schemes, a second-order accurate backward differencing scheme is used for time integration. The time-step size was restricted according to the Courant - Friedrichs - Lewy number

$$CFL = \triangle t \max\left(\frac{|U|}{\triangle x} + \frac{|V|}{\triangle y} + \frac{|W|}{\triangle z}\right) \tag{10}$$

To ensure stability, CFL was set equal to 0.6 to ensure time accurate and stable results. Concerning the spatial discretization, second-order linear schemes were used for both the diffusive and convective fluxes. It should be noted that a detailed study of the fundamental physical processes of turbulence-driven secondary flows would demand the use of a higher-order accurate discretization scheme such as the Spectral Element Method used by Marin et al. [2] to examine the nature of flows in hexagonal ducts. Coupling of the continuity and momentum equations was done iteratively using the PISO algorithm.

The boundary conditions employed were as follows. At the walls, the no-slip condition was applied for the velocities while the wall-normal pressure gradient was set equal to zero. At the outlet, the pressure and the streamwise gradients of the axial velocity were set to zero. At inlet, the internal mapping procedure of de Villiers [18] was used. An arbitrary plane close to the outlet was identified from where the computed velocities were extracted at each time step to be inserted at the inlet. Placing this arbitrary plane at some distance upstream of the outlet prevents spurious errors due to reflections from the outlet from being propagated back to the inlet. In the present work the mapping plane was located at a distance of $6.0D_h$ from the inlet plane; the total length of the channel being $6.4D_h$. Subsequent tests confirmed that the feedback effects were minimal. The mapping length of $6.0D_h$ is in-line with the recommendations of Pallares and Davidson [8] who performed calculations in the same Re_b regime. Other researchers (e.g. Refs. [21,22]) recommended longer domains but preliminary tests showed that this is not necessary.

Several methods for initializing the velocity field were considered. The one which proved most effective in producing a realistic and sustainable turbulence field was the method proposed by de Villiers [18] which is based on the initialization of the velocity field with a transitional-like state. A laminar mean profile (U_0) was superimposed by artificially created streamwise streaks to yield an instantaneous velocity (U) that defines parallel low- and high-speed streaks:

$$U = U_0 + u_\tau\frac{\triangle U^+}{2}\cos(\beta^+ z^+)\frac{y^+}{40}\exp(0.5 - (y^+)^2\sigma)C_{as} \tag{11}$$

where $\triangle U^+ = 0.25U_b/u_\tau$, $\sigma = 5.5 \times 10^{-4}$ and $\varepsilon = U_b/200$. The friction velocity u_τ was estimated using the formulation of Jones [23]. This leads to $\mathrm{Re}_\tau(=u_\tau D_h/2\nu)$ of 196.5 for the case of $\mathrm{Re}_b(=U_b D_h/\nu)$ of 6,000 and $\mathrm{Re}_\tau = 306$ for the case of $\mathrm{Re}_b = 10{,}000$. The value $\beta^+ = 2\pi/200$ determines the spanwise streak spacing. The constant $C_{as} = 1.1$ introduces a small random deviation in order to break the symmetry. Then streak waviness is introduced in order to perturb the streaks and produce streamwise vortices

$$W = \varepsilon\sin(\alpha^+ x^+)y^+\exp(-(y^+)^2\sigma)C_{as} \tag{12}$$

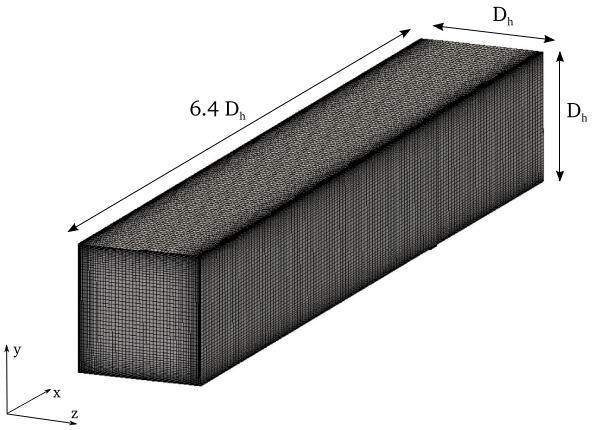

Fig. 1. Computational domain and coordinates system.

where $\varepsilon = U_b/200$ and $\alpha^+ = 2\pi/500$ represent the streamwise spacing.

Calculations were performed for two different Reynolds numbers (based on the bulk velocity U_b) $\mathrm{Re}_b = 6{,}000$, 10,000 for which other LES results are available for comparison. The size of the computational domain is taken to be $6.4\,D_h \times D_h \times D_h$, in the streamwise and cross-stream directions, respectively. Fig. (1) shows the computational domain and a representative grid. Results were obtained on several grids. A detailed assessment of the numerical accuracy is presented in the Appendix.

3. The isothermal flow

A measure of the departures of the instantaneous profiles from their long-time averaged equivalents can be seen in Fig. (2a), where a cross-stream distribution of streamwise velocity is plotted. The departures from the mean values are quite large, and the instantaneous flow does not exhibit the symmetry that is suggested by the averaged profiles.

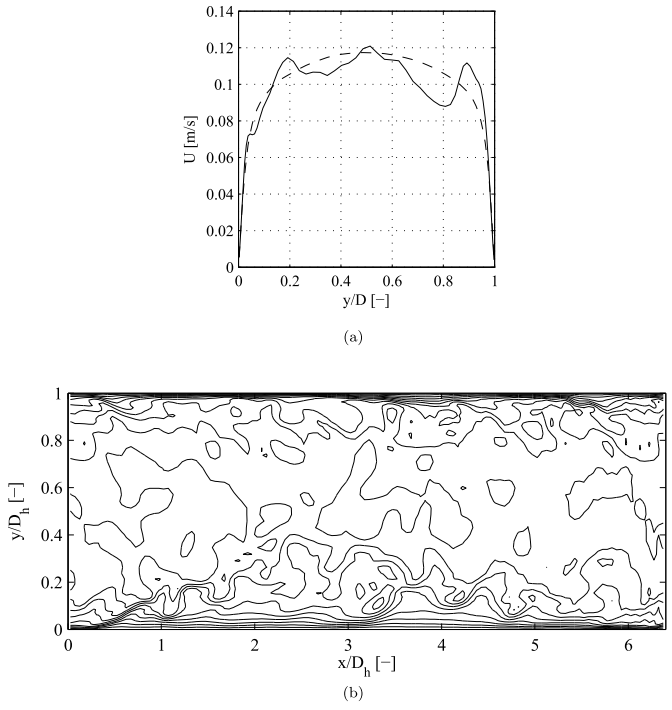

Fig. 2. Streamwise velocity component, (a) along a bisector at $x = 6D_h$, mean value (– –) and instantaneous (—) distribution, (b) velocity contours in a plane normal to z in the middle of the duct.

Contours of the streamwise velocity for a section in the xy-plane are presented in Fig. (2b). These too clearly show the patchy nature of the instantaneous velocity.

Instantaneous snapshots of the secondary flow, taken at four points in time, are shown in Fig. (3). The motions are irregular and the maximum cross velocity occurs in the near-wall region where the turbulence anisotropy is largest.

The results shown here were obtained at $x = 6D_h$. Simulations were performed for a period of 5,000 s before starting the averaging process. In terms of non-dimensional time units $t^+ = tu_\tau^a/D_h$, this time period corresponds to values of t^+ of 30 and 59, for $\mathrm{Re}_b = 6000$ and $\mathrm{Re}_b = 10000$, respectively. The averaging process itself is performed for another 5,000 s. A convenient indicator of whether the flow has become fully developed is the variation of the section-averaged pressure with streamwise distance which should become linear. This was indeed obtained within the averaging interval. The average wall shear stress (τ_w^a), which can be obtained from a simple force balance, turns out to be equal to 3.963×10^{-5} kg m^{-1} s^{-2}.

The variation of the mean streamwise velocity along the bisectors of the four walls is shown in Fig. (4a). The velocity is non-dimensionalised by the centerline value U_0. Also plotted there are the DNS results by Ref. [24]. Some difference with the DNS results are evident, due in part to the latter being at $\mathrm{Re} = 4{,}410$. Fig. (4b) shows isolines of the normalized mean streamwise velocity in a cross-section at $x = 6D_h$. Five isolines are evenly distributed from $\langle U\rangle/\langle U_0\rangle = 0.3$ to 0.9. The slight deformation towards the corners is due to the secondary flow being directed along the corner bisectors.

Details of the secondary flow produced by the stress anisotropy can be seen in Fig. (5a). The small departure from symmetry observed for the mean streamwise velocity in Fig. (4) can also be seen here. Wall tangential motion in the middle of each wall is not entirely zero. In Fig. (5a), this effect is especially visible at the top wall. On average, fluid with higher streamwise velocity is transported from the middle of the duct towards the edges. For mass continuity reasons fluid in the corner close to the wall is driven to the middle of the wall, where it ascends to the duct center. In many papers quadrant averaged results are presented to improve statistics and obliterate a possible lack of symmetry. Therefore, secondary velocity components are spatially averaged over all octants and the results are shown in Fig. (6). The maximum secondary velocity is calculated as $\langle V\rangle_{max}/U_b = \langle W\rangle_{max}/U_b = 1.73\%$ and was found $0.19D_h$ away from the corner at a wall distance of $0.03D_h$. This location is assigned to the area where near-wall fluid travels from the corners back to the mid of the wall. However, fluid particles with the highest magnitude $(\langle V\rangle^2 + \langle W\rangle^2)^{0.5}_{max}/U_b = 1.76\%$ are located on the diagonal at $1.372D_h$ wall distance. The streamwise vorticity is calculated from the velocity-gradient field according to:

$$\omega_x = \frac{\partial W}{\partial y} - \frac{\partial V}{\partial z}. \tag{13}$$

Results for the ω_x distribution normalized by the maximal value of ω_x are shown in Fig. (5b) where the solid isolines represent positive and the dotted isolines negative values. Maximal vorticity of $|\omega_x| = 0.127$ s^{-1} occurs within the wall-closest grid cells. However, local maxima of up to 0.057 s^{-1} can be detected at a wall distance of 0.053 to $0.073D_h$. Detailed analysis of the interconnection between the mean streamwise vorticity, the wall streaks and the buffer layer coherent structures can be found in Pinelli et al. [25].

The secondary motion described above distorts the mean streamwise velocity in vicinity of the wall. Therefore, wall shear stress distribution in spanwise direction is not uniform for flow in a square duct but a function of y and z respectively. The local wall shear stress values are calculated from

$$\tau_w = \mu\left(\frac{\partial U}{\partial n}\right)_w \tag{14}$$

where μ is the dynamic viscosity and n is the wall-normal direction. The

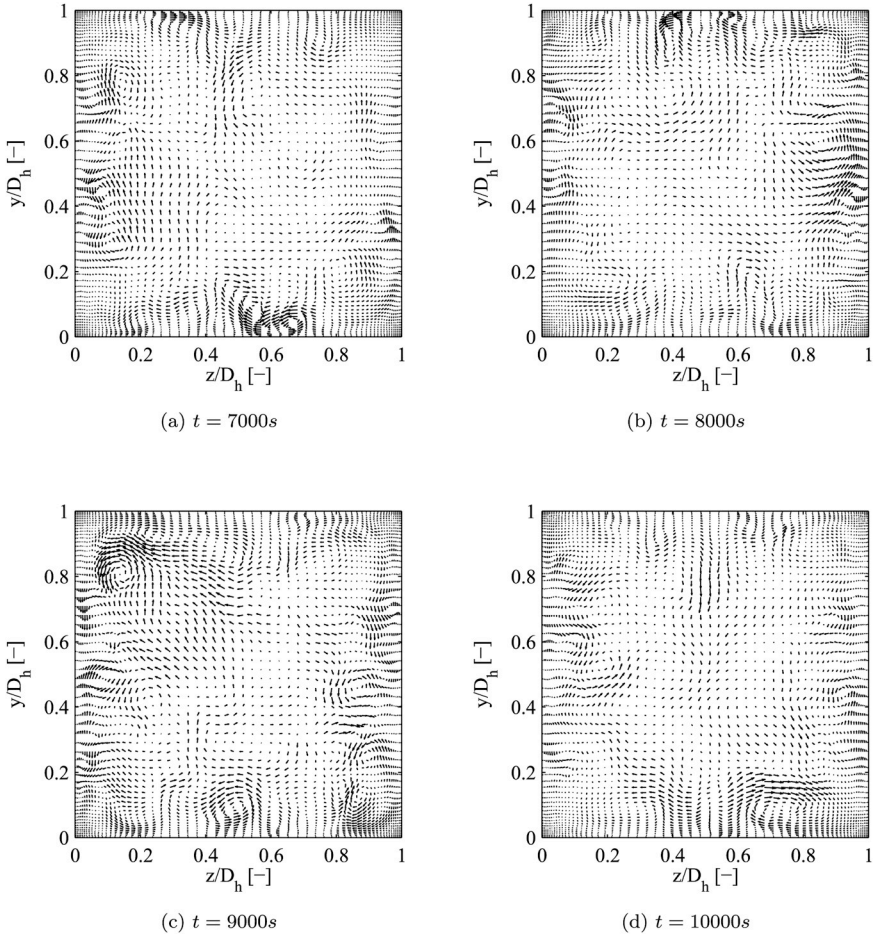

Fig. 3. Instantaneous cross-flow velocity distribution in slices normal to the main flow direction at different times.

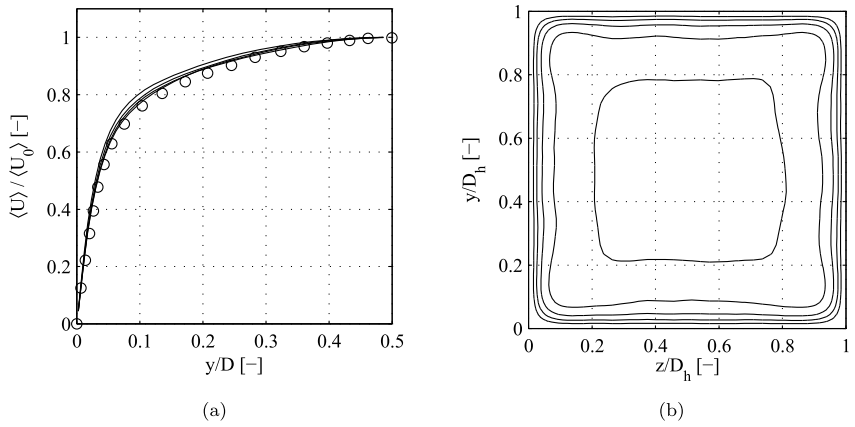

Fig. 4. Mean streamwise velocity distribution, (a) normalized mean streamwise velocity, LES (—), DNS [24] (∘), (b) isolines of normalized mean streamwise velocity $\langle U\rangle/\langle U_0\rangle$.

gradient is evaluated by first-order differencing which is acceptable because of the linear velocity profile in the viscous sublayer. The flow asymmetry has an even stronger impact on the distribution of τ_w. The variation of the ratio τ_w/τ_w^a is shown in Fig. (7a) where the peripheral averaged wall shear stress $\tau_w^a = 3.973 \times 10^{-5}\,\mathrm{kg\,m^{-1}\,s^{-2}}$ fits well with the one calculated from the pressure drop.

The quadrant-averaged shear-stress distributions along the four walls show some differences (Fig. (7a)) which suggests that a longer time-averaging interval might have been appropriate. Vinuesa et al. [21] reported that an averaging time of $t^+ \approx 400$ was needed to achieve statistical convergence but that was for Direct Numerical Simulations (DNS) where flow features are captured in greater detail than in LES. The peak in the center of the wall is lower in comparison to the DNS results [24] but at the same level as the LES results of [9]. The local variation is significantly weaker, though. In vicinity of the corner all results coincide well. The outer peak is located $0.15D_h$ away from the corner. This suggests that it is connected to the area of highest cross-flow velocity.

The wall-normal distance is non-dimensionalized according to $y^+ = (u_{\tau,m}^a y)/\nu$ and the non-dimensional mean streamwise velocity reads $U^+ = \langle U\rangle/U_{\tau,m}^a$. In immediate vicinity of the wall up to $y^+ = 5$ the velocity profile exhibits linear behavior following

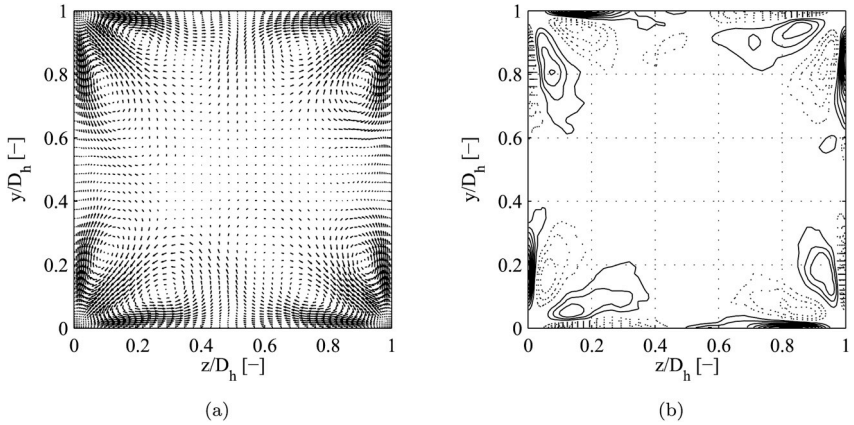

Fig. 5. Secondary flow, (a) cross-stream velocity, (b) streamwise vorticity $\omega_x/\omega_{x,max}$, positive isolines (—), evenly distributed from 0.1 to 0.9 in steps of 0.1, negative counterpart (·····).

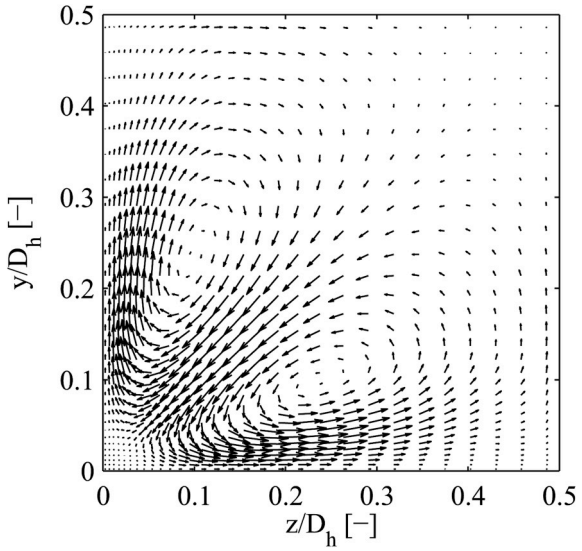

Fig. 6. Secondary velocity vectors, octant averaged.

$$U^+ = y^+. \tag{15}$$

In the viscous sublayer, turbulent transport is negligible because turbulent fluctuations are damped by the presence of the wall. A buffer-layer is adjacent to the viscous sublayer from $5 \leq y^+ \leq 30$. Here, molecular and turbulent transport occur at the same level. Further away from the wall the fully turbulent region starts. Here, molecular properties play a minor role since the turbulent transport dominates. The logarithmic law of the wall which is applicable in this region reads

$$U^+ = \frac{1}{\kappa}\ln(y^+) + C \tag{16}$$

where $\kappa = 0.41$ and the integration constant is chosen to be $C = 5.5$ as it is commonly used for a flat plate boundary layer. The non-dimensionalized mean streamwise velocity U^+ is plotted against y^+ in Fig. (8a). Data by Refs. [24] and [9] is shown for comparison. In the viscous sublayer up to $y^+ = 5$ the velocity profile exhibits the expected linear behavior. In this region data of the present LES coincides well with DNS data. In the turbulent regime the LES results overshoot the values predicted by the law of the wall and by Ref. [24]. A reason for the overshoot of latter is the lower wall shear stress value at the mid-wall (see Fig. (7b)). Note that the deviation is weaker for the friction velocity as it is proportional to the root of the wall shear stress. When comparing results to other works, it is important to keep in mind that different normalization methods are used in literature. To point out this large influence on the illustration, a second plot of the same issue is presented in Fig. (8a). The friction velocity averaged over four walls is obtained as

$$u_\tau^a = \sqrt{\frac{\tau_w^a}{\rho}}. \tag{17}$$

In the turbulent, logarithmic region a closer agreement to Gavrilakis' data [24] is found. An additional DNS data set by Ref. [26] is added which is also well reproduced by LES calculations by Ref. [27]. Their data, obtained for higher Reynolds number flows, differ appreciably. The overshoot from the law of the wall curve, is due to stronger turbulence production close to the wall center compared to simpler boundary layer or channel flows [26].

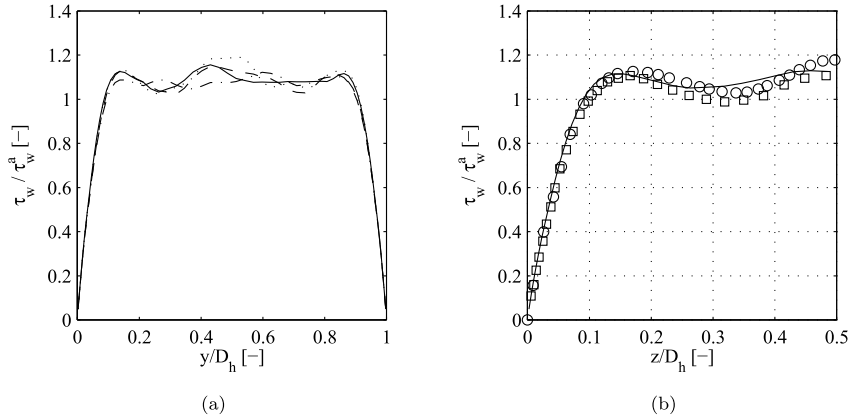

Fig. 7. Non-dimensionalized wall shear stress, (a) separate distributions along each wall of present LES, (b) comparison to DNS [24] (○), LES 9 (□).

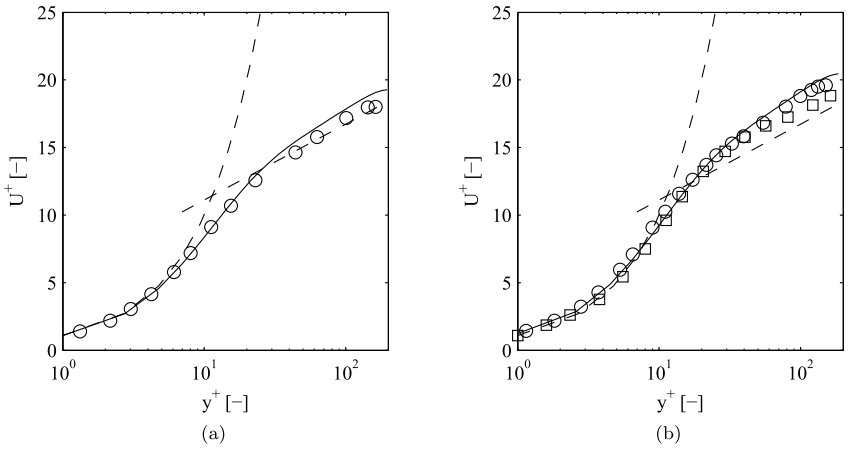

Fig. 8. Comparison of predicted mean streamwise velocity along the wall bisector with law of the wall (– –) and with the DNS results of [24] (∘) and [26] (□); (a) normalized by mid-wall friction velocity and (b) averaged friction velocity.

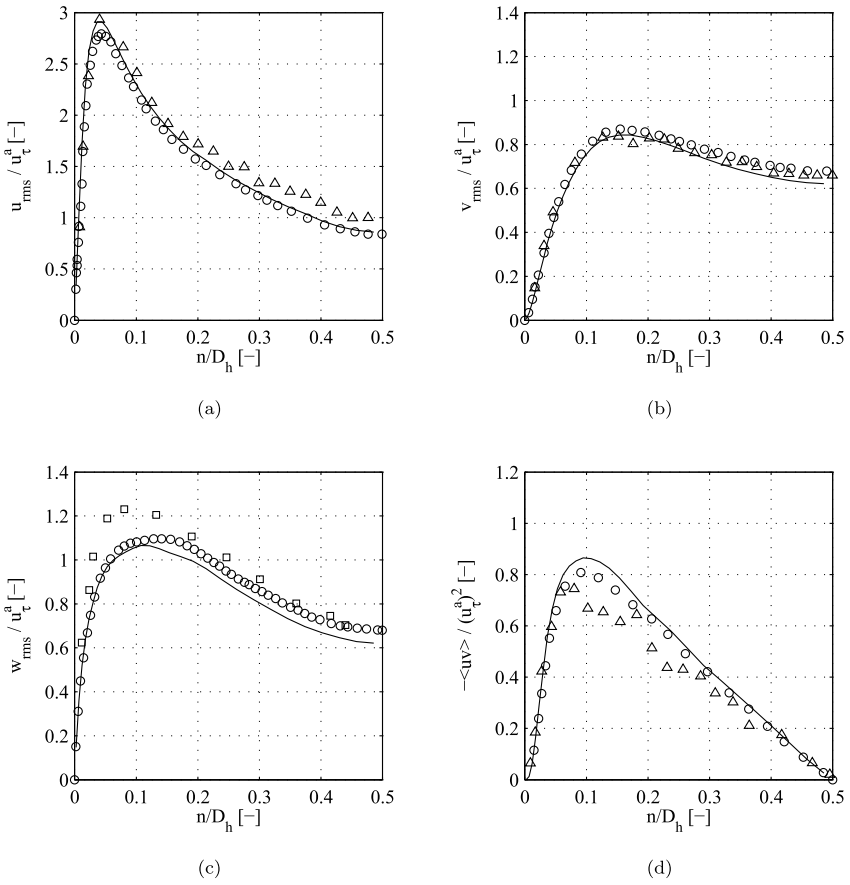

Fig. 9. Comparison of turbulence intensities with the DNS of [24] (∘), and the experimental data of [29] (△) and [28] (□). (a) u_{rms}, (b) v_{rms}, (c) w_{rms}, (d) $-\langle uv\rangle$.

In Figure (9a), the intensity of the quadrant-averaged streamwise velocity fluctuation along the duct bisectors is illustrated. A distinct maximum of streamwise fluctuations occurs in vicinity of the wall at $n = 0.04D_h$. Comparing the present LES results to DNS data [24], a perfect agreement of streamwise intensities u_{rms} is apparent. The maximum value agrees well with experimental channel data [28] whereas the deviation in the far-wall region is higher. LES data for v_{rms} and w_{rms} deviates slightly stronger from DNS data especially towards the duct center where the deviation is up to 9%. Experimental channel data [29] gives a 15% higher peak in w_{rms}, but agrees well with [24] in the duct center. It should be mentioned that [24] used a local mid-wall friction velocity to non-dimensionalize turbulent intensities. He calculates the local friction velocity to $1.09u_\tau^a$. Therefore, data is rescaled in order to provide an appropriate comparison to the present LES data. The variation of Reynolds stress $\langle uv\rangle$ is plotted in Fig. (9d). The present LES result agrees fairly well with DNS data except for an overshoot of the maximum value at $y = 0.1D_h$. It is also located a bit further away from the wall. Experimental data by Ref. [29] exhibits no smooth behavior as in numerical data and Reynolds stresses are in general at a lower level.

4. The heated flow

Computations were performed for two different thermal boundary conditions. The first was that of constant wall temperature, hereafter

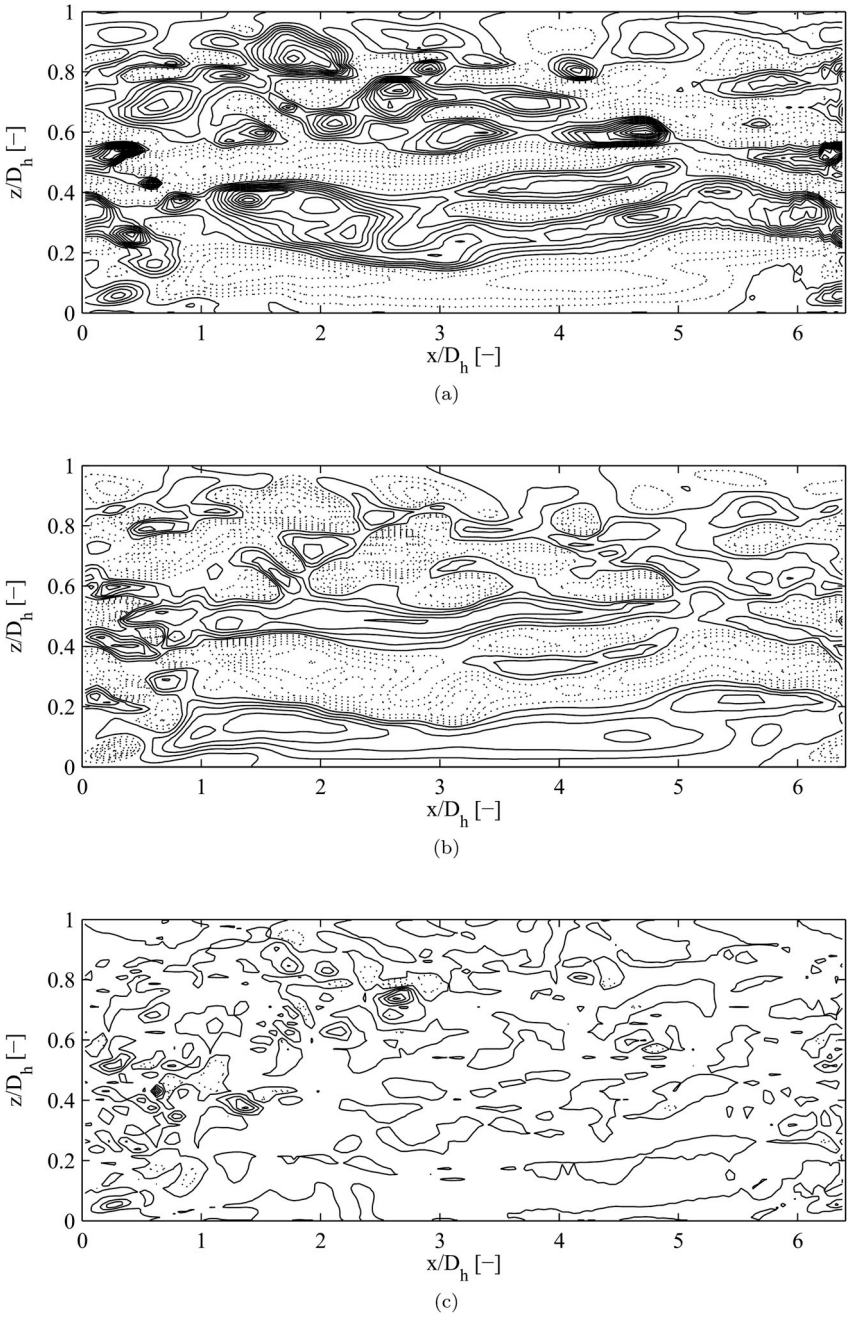

Fig. 10. Contours of instantaneous fields at $y^+ \approx 4.8$ for case h1; positive contours are shown as solid, negative as dotted lines; (a) streamwise velocity fluctuations u^+ from − 2.5 to 5.5 by increments of 0.5, (b) temperature fluctuations θ^+ from − 4.5 to 2 by increments of 0.5, (c) wall-normal heat flux $v^+\theta^+$ from − 0.5 to 1 by increments of 0.2.

referred to as case h1. This corresponded to an initial temperature difference of $\Delta\Theta = 50$ K between the wall temperature and the inlet temperature. The thermal field does not become fully developed and hence the cyclic boundary conditions were not applied. Instead, the inlet temperature was fixed throughout the simulations, and the spatially evolving thermal field was examined. The second was that of constant wall heat flux, referred to as case h2. The heat flux was calculated according to the previous constant wall temperature simulation. The thermophysical fluid properties were constant for both cases. Thus, the fully developed flow field that was generated by the mapping method described above was decoupled from the thermal field.

Contours of instantaneous streamwise velocity fluctuations, temperature fluctuations and wall-normal component heat flux are presented in Fig. (10). The contours were all obtained at the same time, and on the same plane located at distance at $y^+ = 4.8$ from the bottom wall. The strong coupling between the fluctuations in the velocity and temperature fields is quite evident though these seem to be out of phase. The appearance of maxima in the normalized wall-normal heat flux $v^+\theta^+$ seems to be intermittent as can be seen in Fig. (10c). A similarly intermittent behavior is also observed in the contours of u^+v^+ contours where the maxima also appear to be intermittent [30].

The distribution of wall heat flux $\dot{q}_w$ is shown in Fig. (11). Note that the heat flux through the surface is high in regions where high-speed streaks in streamwise velocity appear (Fig. (10a)). This is to be expected since high-speed streaks generate higher levels of wall shear stress and hence, according to Reynolds analogy, higher levels of $\dot{q}_w$.

The spatial evolution of the mean temperature profiles (quadrant averaged) at three streamwise positions is plotted in Fig. (12). Note that

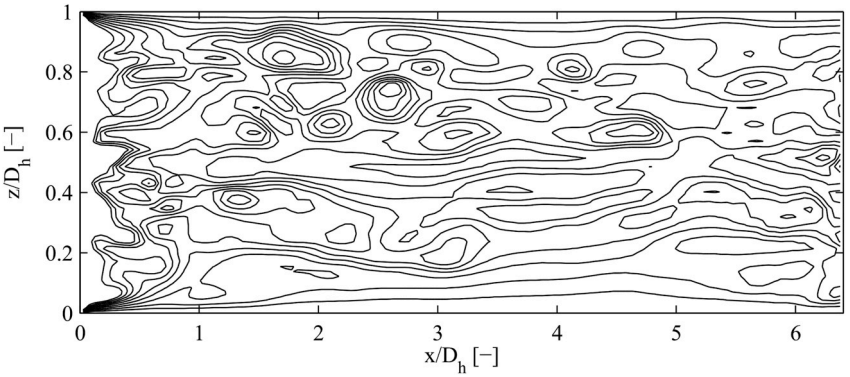

Fig. 11. Contours of instantaneous wall heat flux $\dot{q}_w$ at the bottom wall for case h1, contour levels are from 10 W m^{-2} to 60 W m^{-2} by increments of 6.25 W m^{-2}.

the wall temperature for case h2 (Fig. (12b)) increases linearly in x while its gradient stays constant by definition. At $x = 6D_h$ the constant wall temperature set in case h1 is almost reached, concomitant with a similar mean temperature profile. The predicted development of the thermal field shows that for a constant wall temperature, after a sufficiently long development length, the temperature everywhere will asymptotically aproach that at the wall.

It is instructive to plot the mean temperature in the form of a thermal logarithmic law since the existence of this law often provides the basis for specifying the boundary conditions at a solid wall. To achieve this, the temperature is non-dimensionalized according to

$$\Theta^+ = \frac{\Theta_w - \langle\Theta\rangle}{\Theta_\tau} \tag{18}$$

where

$$\Theta_\tau = \frac{\dot{q}^a_{w,m}}{\rho c_p u^a_{\tau,m}} \tag{19}$$

In the above, $\dot{q}^a_{w,m}$ and $u^a_{\tau,m}$ are the mid-wall heat flux and friction velocity, respectively.

In the viscous sublayer, the mean temperature along the wall-normal bisector is expected to follow the relation

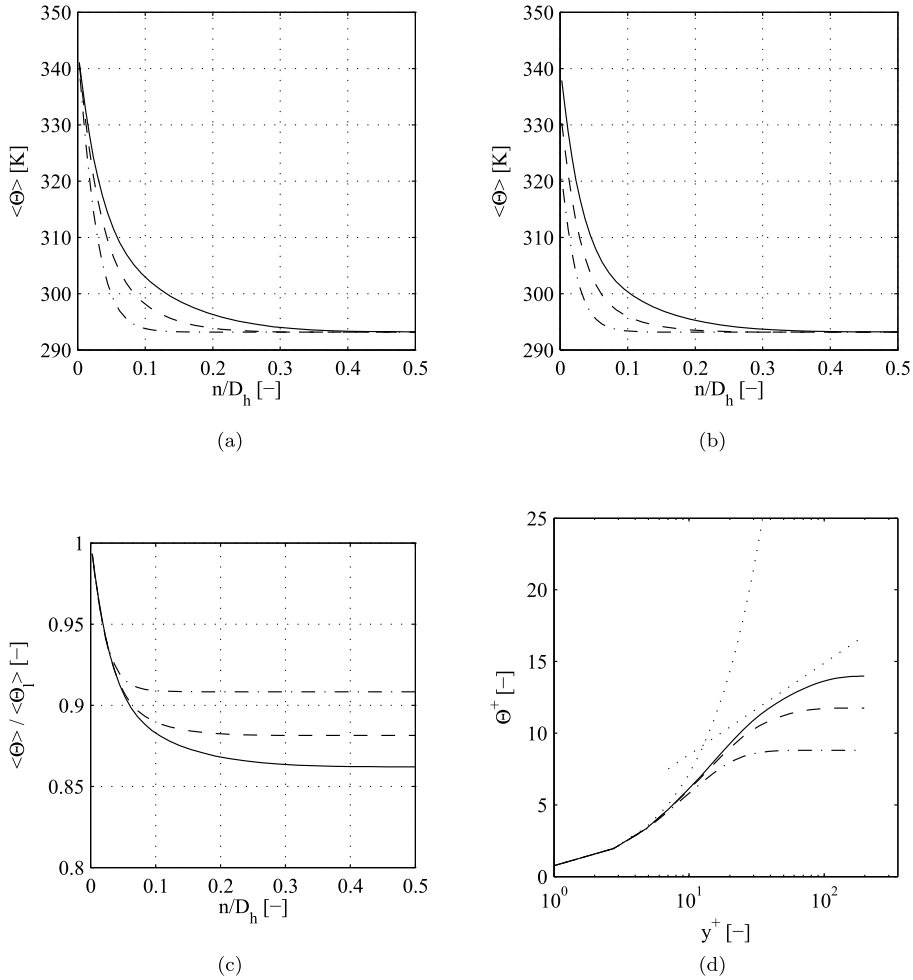

Fig. 12. Mean temperature profiles at $x = 6D_h$ (—), $x = 3D_h$ (– –), $x = 1D_h$ (– –); (a) case h1 with constant wall temperature, (b) case h2 with constant wall heat flux, (c) case h2 non-dimensionalized, (d) case h2 $\Theta^+(y^+)$.

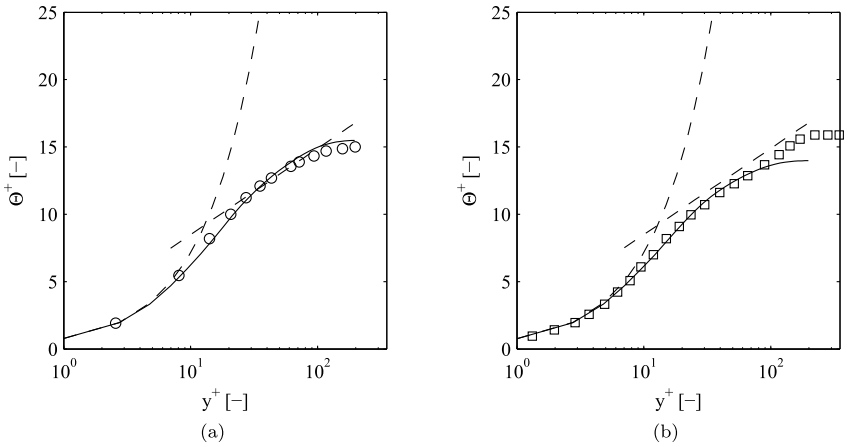

Fig. 13. Non-dimensionalized mean temperature profiles of (a) case h1, (b) case h2; present LES (——), LES by Ref. [27] (∘), DNS by Ref. [31] (□).

$$\Theta^+ = \mathrm{Pr}\, y^+. \tag{20}$$

The results from both h1 and h2 simulations agree well with this relation as well as literature data. In the logarithmic region, the expected relationship reads:

$$\Theta^+ = \frac{\mathrm{Pr}_t}{\kappa} \ln(y^+) + C_\Theta \tag{21}$$

Kong et al. [31] compare their results with $\Theta^+ = 2.075 \ln(y^+) + 4.03$ while Qin and Pletcher [27] use $\Theta^+ = 2.78 \ln(y^+) + 2.09$. The latter is plotted in Fig. (13) where it is compared with the present predictions. Differences between the two sets of results are due in part to slightly different ratio of wall to bulk temperatures (1.23 in Ref. [27], 1.17 here), and in Reynolds number. Fig. (13b) presents the temperature profile for the h2 case. These profiles are in good agreement with the DNS data of [31] for a constant-flux heated flat plate boundary layer.

The heat flux distribution along the wall for the h1 case is shown in Fig. (14a) where it is normalized by its circumferential average. As was the case with the local wall shear stress distribution, two peaks in the heat flux are apparent, one in the middle of the wall and another at $y = 0.15D_h$. Comparison with Fig. (7b) indicates a strong correlation with the local wall shear stress. In the vicinity of the corner, and in the region of the first peak, the present results agree quite well with those of [27], whereas the LES results of [8] show a higher peak that is also shifted away from the corner. The constant flux boundary condition in case h2 produces an axial and peripheral variation of wall temperature while $\dot{q}_w/\dot{q}_w^a = 1$ by definition everywhere. The ratio $(\Theta_l - \Theta^a)/\Theta_\tau$ is shown in Fig. (14b) where Θ_l denotes the local wall temperature, Θ^a the peripheral averaged wall temperature and Θ_τ the friction temperature, defined by Eq. (19). The outer maximum is yet shifted more towards the middle of the wall at $y = 0.2 - 0.25D_h$. In comparison to Qin and Pletcher's [27] LES data temperature in the corner is higher for the present LES, but fits well with [8].

Both h1 and h2 cases have in common that either heat flux is very low or temperature is very high in vicinity of the corner. In a practical cooling application it has to be taken into account that sufficient cooling capability may not be ensured close to the edge. The averaged heat flux is only reached at $y = 0.1D_h$ and further away from the corner. The strong increase of temperature or decrease of heat flux is mainly due to the influence of both perpendicular no-slip walls resulting in a lower streamwise velocity in comparison to a channel flow. The presence of strong secondary motion flow causes the variation of heat transfer along the wall involving a second maximum.

Turning now to consideration of Nusselt number, the streamwise variation of this parameter is shown in Fig. (15). The local Nusselt number is defined as

$$\mathrm{Nu} = \frac{D_h \left(\frac{\partial \langle\Theta\rangle}{\partial n}\right)_w}{\Theta_l - \Theta_b} \tag{22}$$

where Θ_l is the local wall temperature and Θ_b is the bulk temperature:

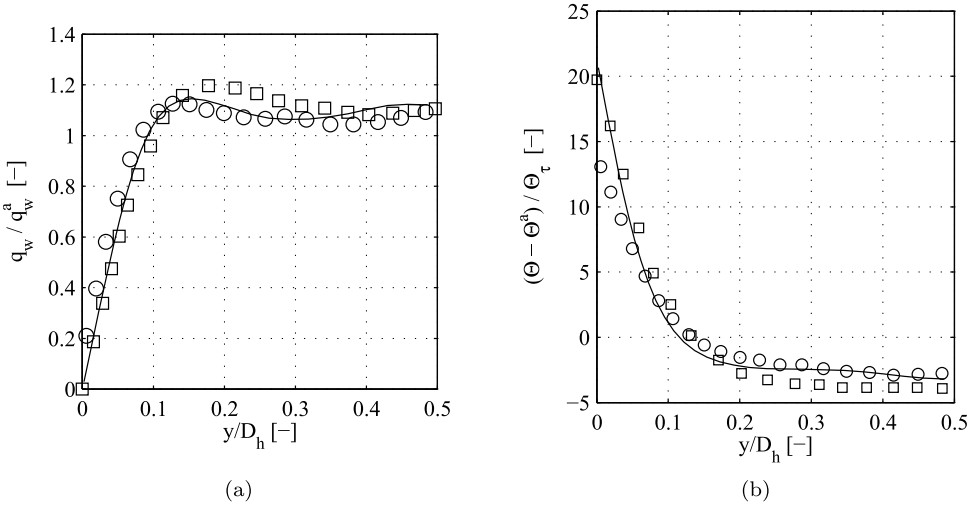

Fig. 14. Predictedl distribution of (a) local wall heat flux in case h1, (b) local wall temperature in case h2; present LES (——), LES by Ref. [27] (∘), LES by Ref. [8] (□).

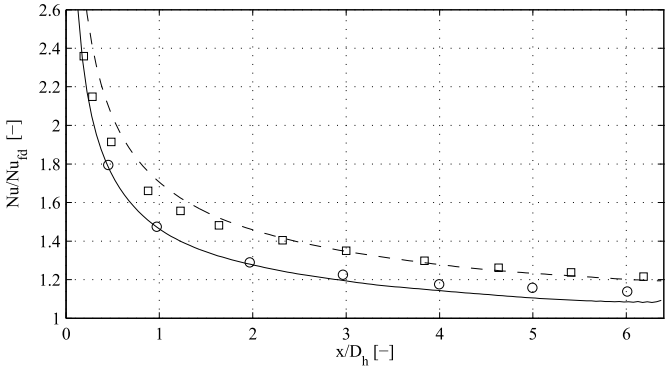

Fig. 15. Local Nusselt number distribution in streamwise direction; comparison of isothermal case h1 (——), isoflux case h2 (– –), LES by Ref. [27] (∘), experimental data by Ref. [33] (□).

$$\Theta_b = \frac{\int_0^{D_h}\int_0^{D_h} \langle\Theta(y,z)\rangle\langle U(y,z)\rangle dydz}{\int_0^{D_h}\int_0^{D_h} \langle U(y,z)\rangle dydz} \tag{23}$$

According to [32,33], Θ_b is calculated as a function of streamwise distance since it increases along that direction due to contineous supply of heat. An extension of the empirical Dittus-Boelter equation [27] was used to calculate a reference, 'fully developed', Nusselt number:

$$\mathrm{Nu}_{fd} = 0.023\,\mathrm{Re}_b^{0.8}\mathrm{Pr}^{0.4}\left(\frac{\Theta_w}{\Theta_b}\right)^{-0.55} \tag{24}$$

The predicted variation of section-averaged Nusselt number with streamwise distance is presented in Fig. (15) where it is compared with the experimental data of [33] and the LES results of [27]. The decrease of Nusselt number of the isothermal case h1 agrees well with [27]. The levels for case h2 are higher and the predictions fit well with the experiments of [33]. This is not visible in Fig. (15) since it is compensated by an also higher fully developed, reference Nusselt number. Sparrow et al. [33] define $\mathrm{Nu} = 1.05\mathrm{Nu}_{fd}$ as identifier for the thermal entrance length. According to this definition the domain length of the present study allows only to model part of the thermal development zone. However, ratio values near by the outlet at $x = 6D_h$ are as low as $\mathrm{Nu}/\mathrm{Nu}_{fd} = 1.085$ and 1.201 respectively.

The present results provide an opportunity to check the validity in this flow of the Reynolds analogy which can be expressed as:

$$\mathrm{St} = \frac{\mathrm{Nu}}{\mathrm{RePr}} = \frac{c_f}{2} \tag{25}$$

where St is the Stanton number. The results for case h1 are listed in Table 1. The results indicate that fully-developed thermal conditions were attained towards the end of the development length.

We next consider the intensity of the temperature fluctuations. Quadrant averaged cross-stream distributions of rms values along the wall bisector at $x = 6D_h$ are shown in Fig. (16). Also plotted there are the DNS results of [30] for a heated channel and those of [27] for a square duct. The temperature fluctuations are non-dimensionalized with averaged Θ_τ. The root mean square value of the fluctuations rises rapidly away from the wall to reach a maxima at $y^+ \approx 20$. This location coincides with the results of [30,31] though the peak value is slightly underestimated. A similar behavior can be detected for case h2 (Fig. (16b)). Note that the rms value at wall for this case is finite with $\theta^+_{rms} = 2$. This value agrees well with the results of [31] and [27] but is lower than the values given by Refs. [34] and [35]. The reason is in part due to the fact that the thermal field here is not as developed as in the previous studies. This is supported by the observation that the profiles at the more upstream location of $x = 3D_h$, also plotted in Fig. (16), show a lower value at the wall.

Table 1
Reynolds analogy for case h1.

x/D_h	Nu_l	$\mathrm{St} = \frac{\mathrm{Nu}}{\mathrm{RePr}}$	$\frac{c_f}{2}$
6	21.4	5.00×10^{-3}	5.10×10^{-3}
5	21.8	5.09×10^{-3}	5.10×10^{-3}
4	22.59	5.28×10^{-3}	5.10×10^{-3}
3	23.65	5.53×10^{-3}	5.10×10^{-3}
2	25.41	5.59×10^{-3}	5.10×10^{-3}
1	29.26	6.84×10^{-3}	5.10×10^{-3}

The streamwise and wall-normal heat flux components are plotted in Fig. (17) for case h1, and in Fig. (18) for case h2. Comparisons are made with the DNS results for a heated channel [30] and the thermal flat plate boundary layer results of [31]. Additional data by Ref. [34] are used for the constant wall heat flux case. Non-dimensionalized values for temperature fluctuations $\theta^+ = \theta/\Theta_\tau$ and velocity fluctuations $u^+ = u/u^a_\tau$ are used. The streamwise heat flux predictions for case h1 agree very well with both channel flow [30] and flat plate boundary layer [31]. In the outer region, the streamwise heat flux of [30] is slightly higher in comparison to the present results.

Since the plotted value represents the ratio of streamwise heat flux to surface heat flux [30], the corresponding correlation coefficient (Fig. (17b)) reveals a high correlation of up to 0.97 nearby the wall. Up to a distance of $0.3D_h$ from the wall, the slope is in accordance with [30]. Wall-normal turbulent heat flux is considerably smaller than its streamwise counterpart and its maximum is shifted away from the wall (Fig. (17c)). The results of [30] are matched well for $y^+ \leq 50$, especially with regards to the maximum value. The correlation coefficient in Fig. (17d) overshoots, but the trend is otherwise correctly reproduced. The maximum of the turbulent streamwise heat flux for the constant wall heat flux is underestimated, as can be seen in Fig. (18a). Nevertheless, it fits fairly well with the boundary layer data [31]. The correlation coefficient looks similar to that of case h1 but is lower in vicinity of the wall.

Finally, we consider the wall-normal distribution of the turbulent Prandtl number, shown in Fig. (19). This parameter is calculated from:

$$\mathrm{Pr}_t = \frac{-\overline{uv}/(\partial U/\partial y)}{-\overline{v\theta}/(\partial\Theta/\partial y)} \tag{27}$$

The importance of Pr_t stems from its use in turbulence closures to relate the thermal diffusivity to the eddy viscosity. Often, Pr_t is set to a constant value in the range 0.85–1.0. The Prandtl number deduced from the present results suggests a strong dependence on the wall-normal distance. The results for case h1 (Fig. (19a)) show that this parameter has a finite value at the wall, thereafter remaining fairly constant before dropping quite rapidly close to the duct centerline. In contrast, for case h2 (Fig. (19b)), Pr_t is zero at the wall thereafter rising quite rapidly. This trend is supported by the DNS results of [31] and [34].

5. Conclusions

The fully developed turbulent flow through an isothermal and a heated square duct was investigated using Large-Eddy Simulations. Among the computational aspects considered were the implementation of appropriate cyclic boundary conditions that do not introduce aliasing errors, the initialization of the velocity field to rapidly achieve a sustainable turbulence field, and grid effects both in terms of overall density and near-wall resolution. Two-point correlations were evaluated to confirm that the results obtained were independent of the duct length - an incorrect specification of this parameter was found to produce incorrect shear-stress distributions, instabilities in the mean velocity profiles, and erroneous predictions of the cross-flow turbulent fluctuations.

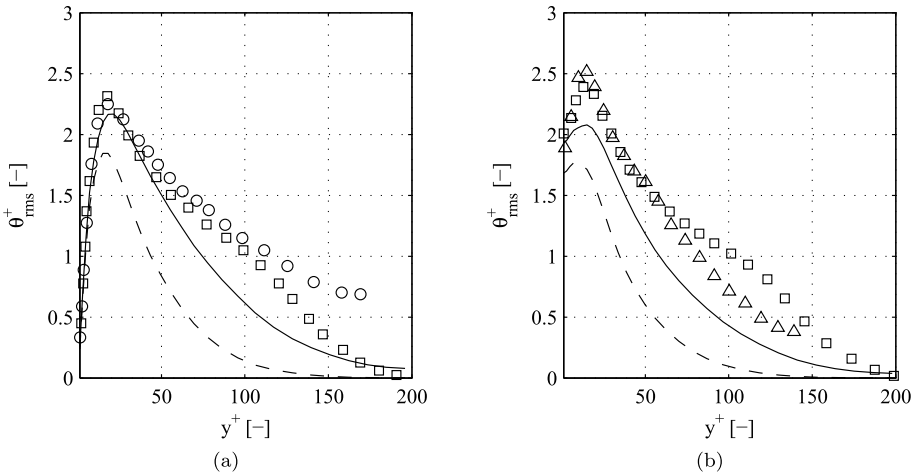

Fig. 16. Profiles of rms temperature fluctuations of (a) constant wall temperature case h1, (b) constant heat flux case h2; present LES at $x = 6D_h$ (——) and at $x = 3D_h$ (– –), LES by Ref. [27] (△), DNS by Ref. [30] (∘), DNS by Ref. [31] (□).

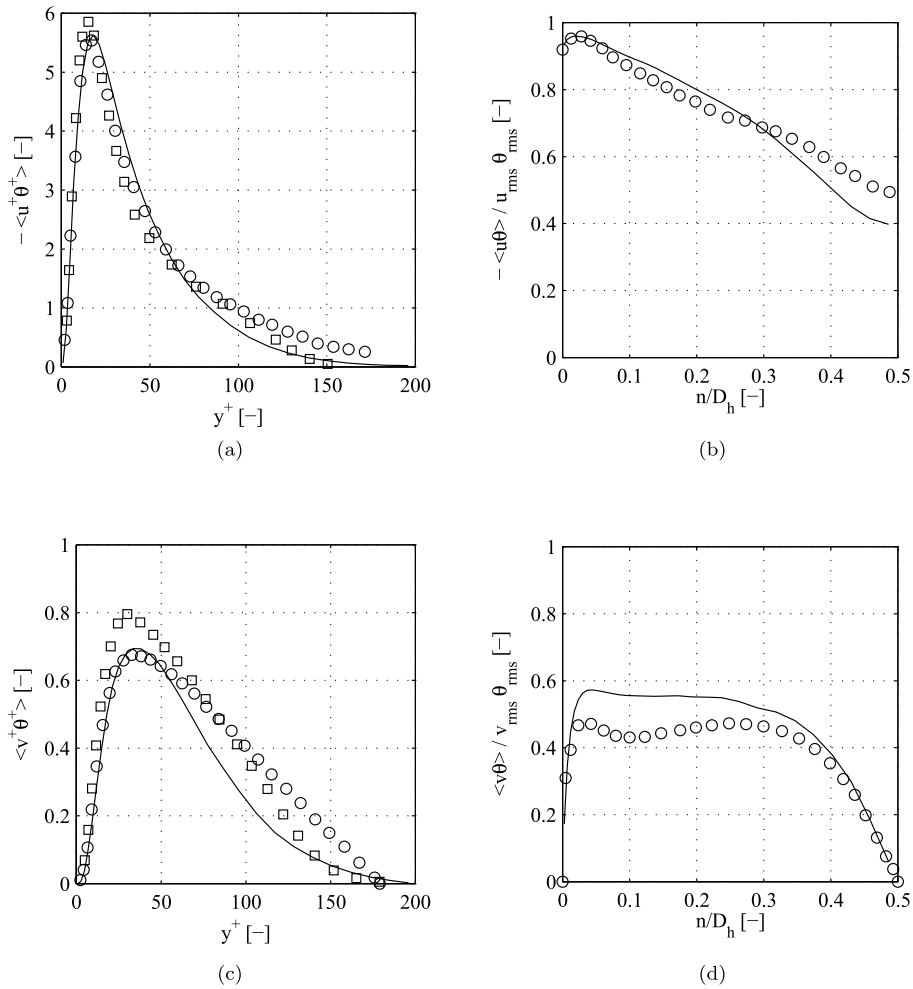

Fig. 17. Case h1: profiles of (a) streamwise heat flux and (b) its correlation coefficient, (c) the normal heat flux and (d) its correlation coefficient; present LES (——), DNS by Ref. [30] (∘), DNS by Ref. [31] (□).

The isothermal flow results, which were obtained to check the accuracy of the present approach, were in accordance with both experimental findings as well as with results obtained using Direct Numerical Simulations. Computations on the finest mesh with the Smagorinsky constant set equal to zero produced no discernible differences compared to results with this constant assigned its usual value. The practice of establishing cyclic boundary conditions between the inlet to the computational domain and a plane displaced upstream of the exit plane ensured that aliasing errors were minimized as evidenced by the distribution of the two-point velocity correlations.

For the heated flows, computations were performed for a developing thermal field in conditions of fully-developed flow. Two thermal

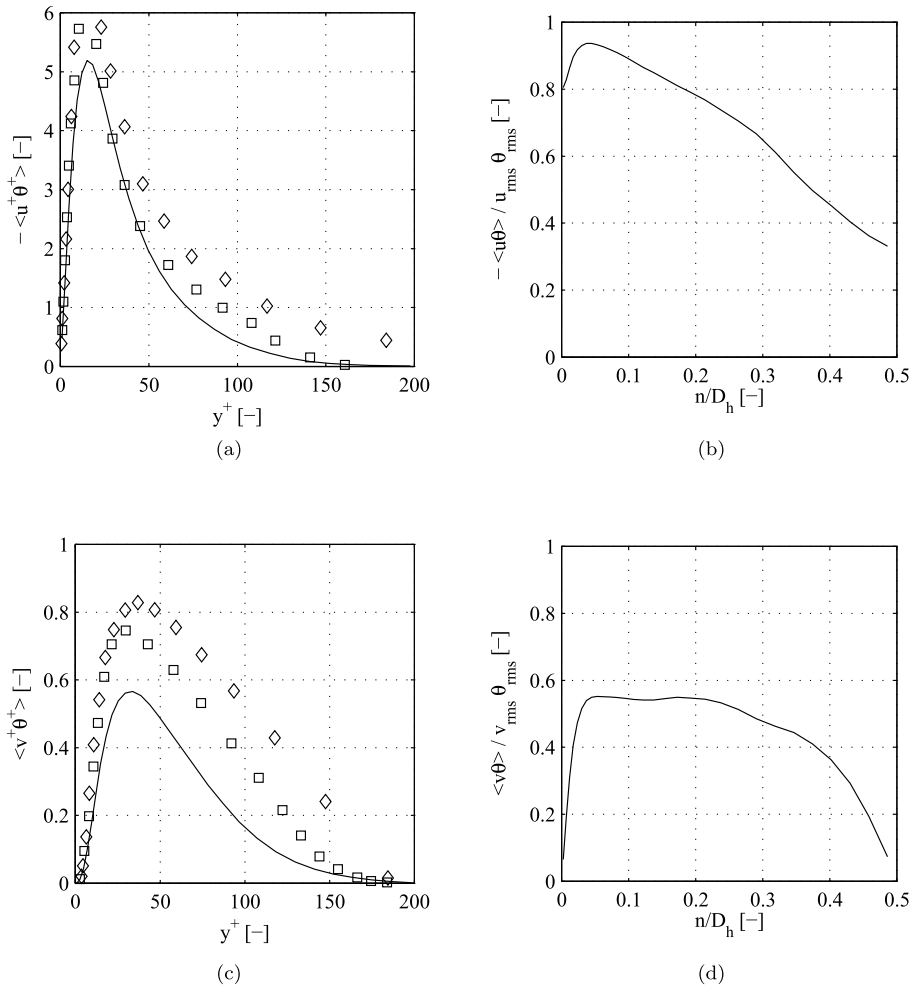

Fig. 18. Case h2: profiles of (a) streamwise heat flux and (b) its correlation coefficient, (c) the normal heat flux and (d) its correlation coefficient; present LES (——), DNS by Ref. [31] (□), DNS by Ref. [34] (⋄).

$$\left\langle u^+\theta^+ \right\rangle = \frac{\overline{u\theta}}{u_\tau \Theta_\tau} = \frac{\overline{u\theta}\rho c_p}{\dot{q}_w}, \tag{26}$$

boundary conditions were examined: constant wall temperature, and uniform constant wall heat flux. It was found that the fluctuating velocity and temperature fields were strongly correlated with high levels of wall heat flux occurring in regions where high-speed streaks in the streamwise velocity appear. It was also found that the distribution of averaged temperature for both cases of constant wall temperature and constant wall heat flux followed an appropriately-defined logarithmic law of the wall - an important finding in the context of RANS closures where this assumption forms the basis of the 'wall functions' approach to specifying the boundary conditions at the wall. Another finding that

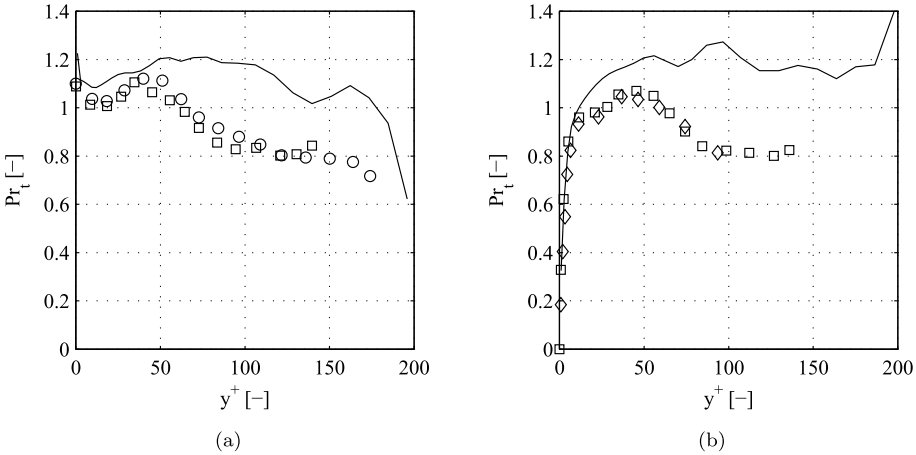

Fig. 19. Profiles of turbulent Prandtl number of (a) case h1, (b) case h2; present LES (——), DNS by Ref. [31] (□), DNS by Ref. [34] (⋄), DNS by Ref. [30] (∘).

is relevant to RANS closures is that the turbulent Prandtl number, while not constant across the entire width of the duct, varies only very marginally in the fully-turbulent region of the flow and thus the assumption of constant value for this parameter that is frequently involved may not be too wide off the mark. What is clear, however, is that the use of Fourier's law in RANS is not supported by the present findings which, in agreement with DNS results, show that the streamwise component of heat flux is 4–5 times greater than the cross-stream component i.e. the heat flux in the direction of the temperature gradient. In this flow, Fourier's law would obtain the streamwise component as being vanishingly small.

Acknowledgement

A. S. gratefully acknowledges the financial support provided by the Erich-Becker Foundation that facilitated his stay at UC Davis. The computations were performed on the Stampede system at TACC/UT Austin, accessed via the XSEDE program.

Notation

Latin Symbols		
c_p	J kg^{-1}K^{-1}	Specific heat capacity at constant pressure
c_f	–	Friction coefficient
D_h	m	Hydraulic diameter
k	W m^{-1}K^{-1}	Thermal conductivity
L_m	m	Mapping position
Nu	–	Nusselt number
n	m	Wall-normal distance
P_w	–	Wetted perimeter
P	kg m^{-1} s^{-2}	Pressure
Pr	–	Prandtl number
$\dot{q}$	W m^{-2}	Heat flux
R_{uu}	–	Correlation coefficient
Re_b	–	Bulk Reynolds number
r	–	Grid stretching factor
S_{ij}	s^{-1}	Strain tensor
St	–	Stanton number
t	s	Time
$U_i = U, V, W$	m s^{-1}	Grid-scale velocity components
$u_i = u, v, w$	m s^{-1}	Grid-scale velocity fluctuations
U_b	m s^{-1}	Bulk velocity
u_τ	m s^{-1}	Friction velocity
$x_i = x, y, z$	m	Cartesian coordinates
Greek Symbols		
$\alpha^+,\ \beta^+$	–	Constants for streak spacing
β	K^{-1}	Thermal expansion coefficient
Γ	m^2 s^{-1}	Thermal diffusivity
$\Delta_{x,y,z}$	m	Cell size
Θ	K	Temperature
Θ_τ	K	Friction temperature
Θ_w	K	Wall temperature
θ	K	Temperature fluctuation
κ		Von Kármán constant
μ	kg m^{-1} s^{-1}	Dynamic viscosity
ν	m^2 s^{-1}	Kinematic viscosity
ω	s^{-1}	Vorticity
ρ	kg m^{-3}	Density
τ_w	kg m^{-1} s^{-2}	Wall shear stress

Appendix. Numerical accuracy

Grid resolution and sub-grid scale modeling

The effects of grid resolution were quantified by performing computations on three different grids whose properties are given in Table 2. The table also gives the near-wall grid sizes, presented in non-dimensional form (e.g. $\Delta_x^+ = u_\tau \Delta_x/\nu$), and the value of the ratio r of adjacent cells in the normal and tangential directions. For cases 1 to 3, the grid resolution in x-direction was unchanged with refinement being applied in the two spanwise directions. For case 4, the refinement is applied in the x-direction. Cases 6 and 7 designate simulations that were performed without using a sub-grid scale model. Note that $\Delta_{x,n,t}^+$ in Table 2 are calculated for each case with the actual maximum wall shear stress. For each case considered, the simulations were started separately from a clear initial field in order to exclude any possible 'memory' effects. The time step was limited by the CFL stability condition. For cases 1 and 2, it is set to $\Delta t = 0.125$ s. For cases 3 and 4 the time step is $\Delta t = 0.0625$ s to meet this requirement. To exclude time-step size effects, case 1 was repeated with the time step halved with no discernible differences being observed.

Table 2
Details of the computational grids.

Case	Grid	No. of cells	Δ_x^+	Δ_n^+	Δ_t^+	r
Case 1	128 × 60 × 60	460800	20.76	1.83	11.60	1.09
Case 2	128 × 100 × 100	1280000	22.06	1.94	5.22	1.05
Case 3	128 × 128 × 128	2097152	22.23	1.96	3.82	1.025
Case 4	256 × 60 × 60	921600	10.28	1.80	11.48	1.09
Case 6	128 × 100 × 100	1280000	21.93	1.93	5.19	1.05
Case 7	128 × 60 × 60	460800	20.70	1.82	11.56	1.09

The outcome of these tests is summarized in Table 3.

Table 3
Summary of results obtained with different grids.

Case	$\langle U \rangle_{max}/U_b$	$\langle V \rangle_{max}/U_b$	τ_w^a [kg m^{-1} s^{-2}]	$\tau_w^{a,m}$ / τ_w^a
Case 1	1.295	1.73%	4.470×10^{-5}	1.13
Case 2	1.296 (+0.1%)	2.00%	4.495×10^{-5} (+0.6%)	1.16
Case 3	1.289 (−0.5%)	2.11%	4.593×10^{-5} (+2.7%)	1.14
Case 4	1.302 (+0.5%)	1.71%	3.887×10^{-5} (−13%)	1.15
Case 6	1.297 (+0.2%)	2.07%	4.552×10^{-5} (+1.8%)	1.13
Case 7	1.297 (+0.2%)	1.76%	4.078×10^{-5} (−8.8%)	1.09

The quadrant-averaged non-dimensional velocity U^+ is plotted along the bisector in Fig. (20a). The results for cases 1 and 4 are indistinguishable which indicates that refining the cells in x-direction further than $\Delta_x^+ \approx 20$ does not improve the results. The variation of wall shear stress averaged over all four walls is illustrated in Fig. (20)b. As expected, cases 1 and 4 yield essentially identical results. Both finer grids depart from the coarser grids such that their outer maxima are shifted towards the corner and exhibit a lower level. Cases 2 and 3 agree fairly well with minor deviations showing a trend that the outer maximum shifts the further to the corner the finer the grid is. Mid-wall values are all at a comparable level.

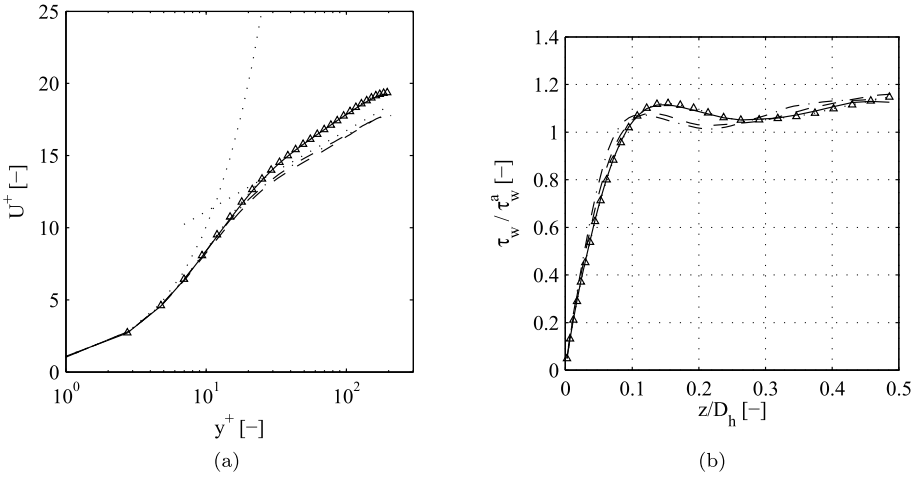

Fig. 20. Comparison of different grid resolutions, case 1 (——), case 2 (– –), case 3 (–·–), case 4 (△)), (a) $U^+(y^+)$, (b) τ_w/τ_w^a.

A closer examination of the grid effects can be seen in Fig. (21) where the turbulent stresses are compared. It is evident that the streamwise turbulence intensity u_{rms} decreases with increasing grid resolution. A similar behavior was identified by Ref. [26] in their DNS results. In contrast, v_{rms} and w_{rms} increase with increasing grid resolution. It should be noted that the size of the cells in contact with the walls remained unchanged for all cases. Only stretching and therefore tangential extent as well as resolution in the duct center differ because of a different cell number.

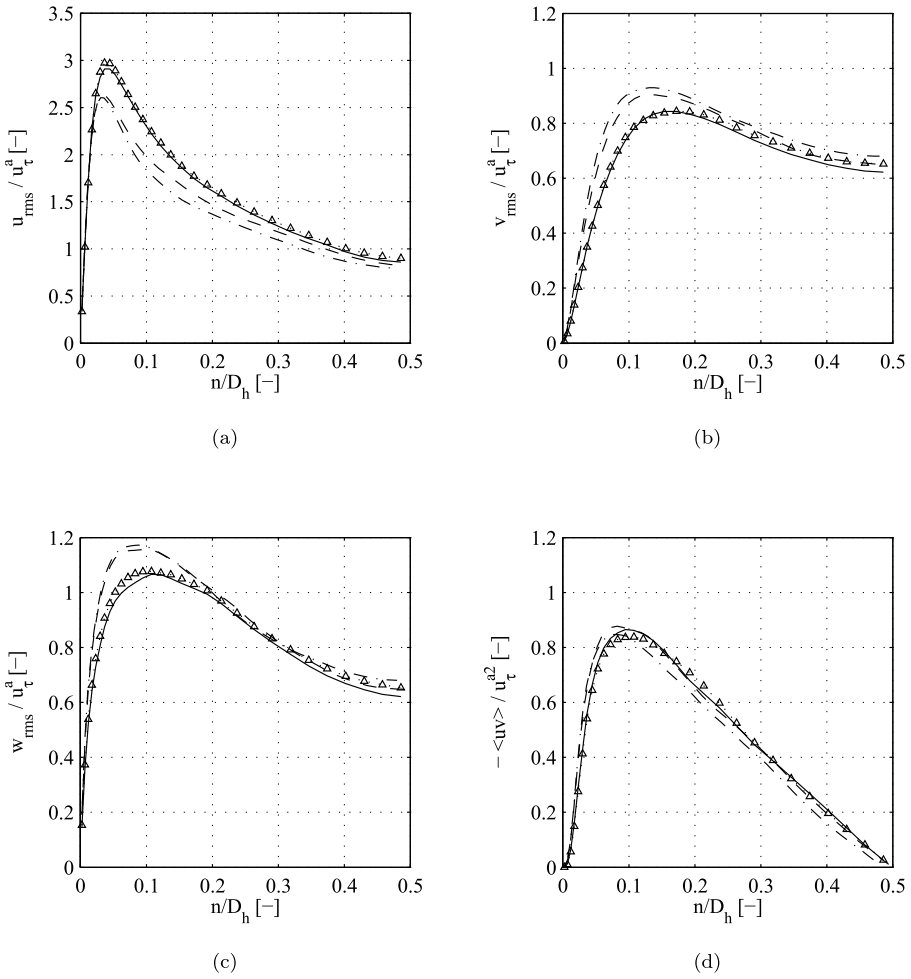

Fig. 21. Turbulent stresses as obtained on different grid resolutions, case 1 (——), case 2 (– –), case 3 (-·-), case 4 (△)), (a) u_{rms}, (b) v_{rms}, (c) w_{rms}, (d) $-\langle uv \rangle$.

The resolution of the fine grids is comparable to and in some cases finer than of some previous DNS studies. [26], for example, uses 96 × 100 × 100 and 64 × 81 × 81 grid points at higher Reynolds numbers of Re_b = 10,320 and Re_b = 10,620 respectively [24]. uses 1000 × 127 × 127 grid intervals for a longer duct at Re_b = 4,410. This corresponds to a non-dimensional grid spacing of $\Delta_x^+ = 9.4$ and $0.45 \leq \Delta_{y,z}^+ \leq 4.6$ [13]. mentions that there is no need for the wall-closest cell to be smaller than $\Delta_y^+ \approx 2$. Therefore, especially the highly resolved cases 2 and 3 can be seen as a kind of DNS since all turbulent motions are supposed to be resolved. If this is the case, sub-grid scale influences should be vanishing. For this purpose two additional simulations were performed. Case 6 has the same settings as case 2, but the Smagorinsky constant C_S is set to zero. This will be referred to below as the no sub-grid scale model. Analogously case 7 is the no SGS counterpart to case 1.

Plotting U^+ over y^+ shows no noticeable difference. Deviation of cases 7 and 1 is always smaller than 2%, deviation of cases 6 and 2 always smaller than 1.1%. Distribution of wall shear stress along the wall differs significantly though. Fig. (22a) unveils that results for the coarser grid differ severely when no sub-grid scale model is used. Moreover, the simulation without sub-grid scale model produces another maximum at $y \approx 0.35 D_h$ while a local minimum occurs at the middle of the wall. The finer cases 2 and 6 agree clearly better.

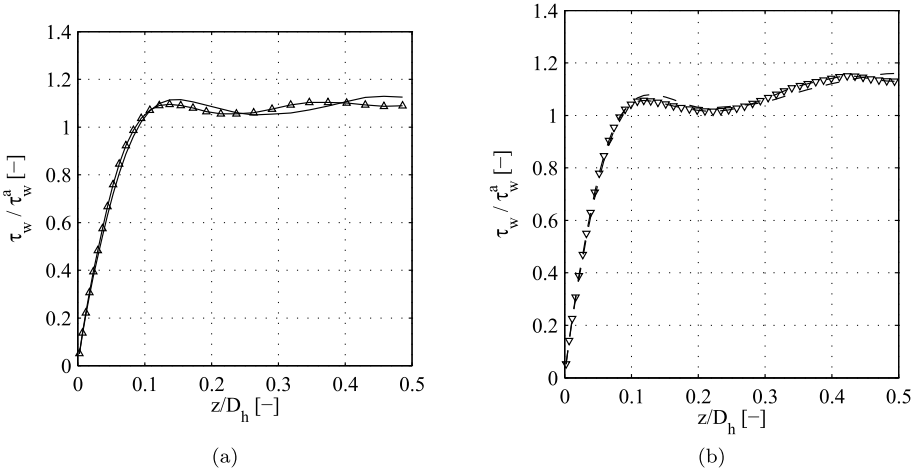

Fig. 22. Comparison of simulations with sub-grid scale (——,– –) and without sub-grid scale model (△, ▽); (a) cases 1 (—) and 7 (△), (b) cases 2 (– –) and 6 (▽).

Two-point correlations

Two-point velocity correlations were evaluated in order to verify that the duct is sufficiently long for the flow field to develop in the central portion of the channel in a way that is not influenced by numerical artifacts associated with the use of cyclic boundary conditions. The correlation coefficients are defined by

$$R_{ii}(r) = \frac{\langle u_i(x)u_i(x+r)\rangle}{(\langle u_i(x)^2\rangle\langle u_i(x+r)^2\rangle)^{0.5}}. \tag{28}$$

Although the correlation coefficients were evaluated at several locations within the flow field, the results at only two such locations with the coordinates $y = z = 0.514D_h$ and $y = z = 0.053D_h$ are presented here. These coefficients are plotted in Fig. (23a) where it can be seen that all the three velocity components in the duct center become effectively de-correlated within a streamwise distance equivalent to one hydraulic diameter from the inlet and outlet planes. Closer to the corner, the streamwise velocity component is stronger correlated as depicted in Fig. (23b). This emphasizes the necessity of a cycling length $L_m \geq 6D_h$. Since the velocity field is extracted from the plane at $x = 6D_h$ and is directly mapped back to the inlet, the correlation coefficients at these two planes are unity by definition.

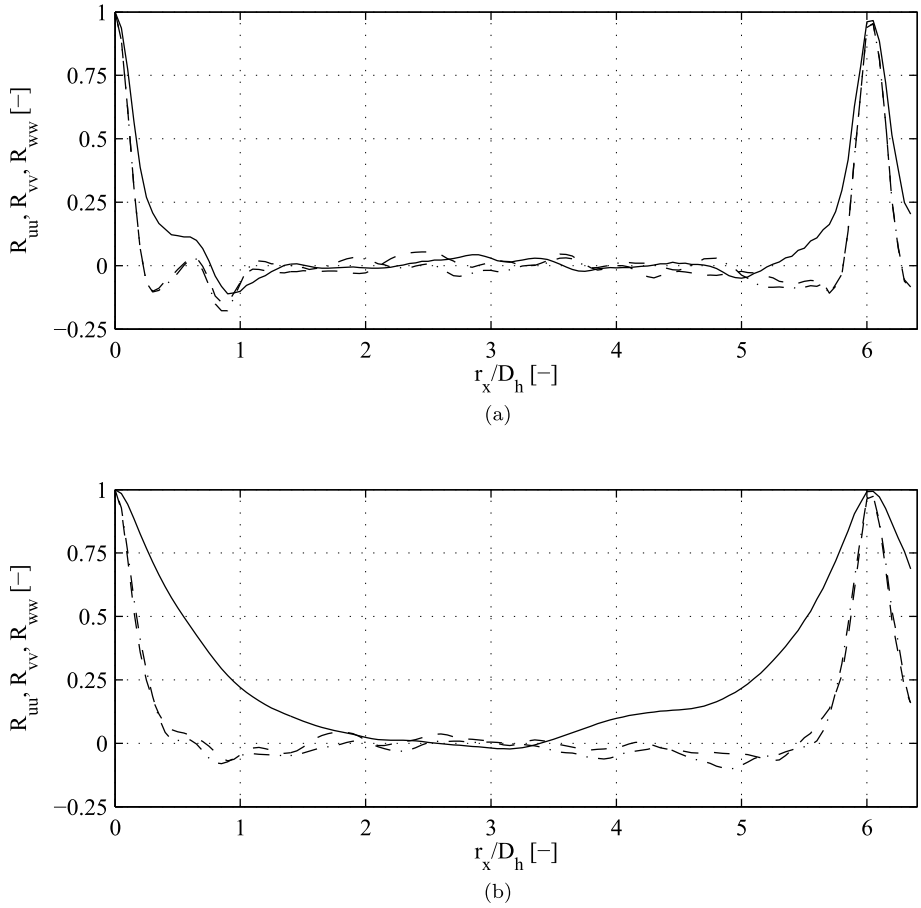

Fig. 23. Two-point velocity correlation coefficients, u (——), v(– –), w(-·–); (a) $y = z = 0.514D_h$, (b) $y = z = 0.053D_h$.

References

[1] E. Battista, H.C. Perkins, Turbulent heat and momentum transfer in a square duct with moderate property variations, Int. J. Heat Mass Tran. 13 (6) (1970) 1063–1065 https://doi.org/10.1016/0017-9310(70)90172-9.

[2] O. Marin, R. Vinuesa, A.V. Obabko, P. Schlatter, Characterization of the secondary flow in hexagonal ducts, Phys. Fluids 28 (2016) 125101 https://doi.org/10.1063/1.4968844.

[3] B.A. Younis, Prediction of turbulent flows in rotating rectangular ducts, J. Fluid Eng. 115 (4) (1993) 646–652.

[4] C.G. Speziale, R.M.C. So, B.A. Younis, On the Prediction of Turbulent Secondary Flows, (1992) NASA CR 189722. ICASE Report No. 92-57.

[5] D. Cokljat, B.A. Younis, Second-order closure study of open-channel flows, J. Hydraul. Eng. 121 (2) (1995) 94–107 https://doi.org/10.1061/(ASCE)0733-9429(1995)121:2(94).

[6] R.K. Madabhushi, S. Vanka, Large eddy simulation of turbulence-driven secondary flow in a square duct, Phys. Fluid. Fluid Dynam. 3 (11) (1991) 2734–2745 https://doi.org/10.1063/1.858163.

[7] M. Breuer, W. Rodi, Large-eddy simulation of turbulent flow through a straight square duct and a 180 degree bend, in: P.R. Voke, L. Kleiser, J.P. Chollet (Eds.), Direct and Large-Eddy Simulation I. Fluid Mechanics and its Applications, 26 Springer, Dordrecht, 1994, pp. 273–285 https://doi.org/10.1007/978-94-011-1000-6_24.

[8] J. Pallares, L. Davidson, Large-eddy simulations of turbulent heat transfer in stationary and rotating square ducts, Phys. Fluids 14 (8) (2002) 2804–2816 https://doi.org/10.1063/1.1489684.

[9] M.S. Vázquez, O. Métais, Large-eddy simulation of the turbulent flow through a heated square duct, J. Fluid Mech. 453 (2002) 201–238 https://doi.org/10.1017/S0022112001006887.

[10] Z. Qin, R.H. Pletcher, Large-eddy simulation of turbulent heat transfer in a rotating square duct, Int. J. Heat Fluid Flow 27 (3) (2006) 371–390 https://doi.org/10.1016/j.ijheatfluidflow.2006.01.003.

[11] Z. Zhu, H. Yang, T. Chen, Numerical study of turbulent heat and fluid flow in a straight square duct at higher Reynolds numbers, Int. J. Heat Mass Tran. 53 (1–3) (2010) 356–364 https://doi.org/10.1016/j.ijheatmasstransfer.2009.09.021.

[12] R. Vinuesa, P. Schlatter, H.M. Nagib, Secondary flow in turbulent ducts with increasing aspect ratio, Physical Review Fluids (3) (2018), https://doi.org/10.1103/PhysRevFluids.3.054606 054606.

[13] J. Fröhlich, Large Eddy Simulation Turbulenter Strömungen 1 Springer, Teubner,

2006.
[14] B. Galperin, S.A. Orszag, Large-eddy Simulation of Complex Engineering and Geophysical Flows, Cambridge University Press, Cambridge, 1993.
[15] J. Smagorinsky, General circulation experiments with the primitive equations: I. The basic experiment, Mon. Weather Rev. 91 (3) (1963) 99–164 https://doi.org/10.1175/1520-0493(1963)091 < 0099:GCEWTP > 2.3.CO;2.
[16] P. Moin, J. Kim, Numerical investigation of turbulent channel flow, J. Fluid Mech. 118 (1982) 341–377 https://doi.org/10.1017/S0022112082001116.
[17] J.W. Deardorff, On the magnitude of the subgrid scale eddy coefficient, J. Comp. Physiol. 7 (1) (1971) 120–133 https://doi.org/10.1016/0021-9991(71)90053-2.
[18] E. de Villiers, The Potential of Large-eddy Simulations for the Modelling of Wall Bounded Flows, PhD Thesis Univ. of London, 2006.
[19] T.M. Eidson, Numerical simulation of the turbulent Rayleigh-Bnard problem using subgrid modelling, J. Fluid Mech. 158 (1985) 245–268 https://doi.org/10.1017/S0022112085002634.
[20] G. Grötzbach, M. Wörner, Direct numerical and large-eddy simulations in nuclear applications, Int. J. Heat Fluid Flow 20 (3) (1999) 222–240 https://doi.org/10.1016/S0142-727X(99)00012-0.
[21] R. Vinuesa, C. Prus, P. Schlatter, H.M. Nagib, Convergence of numerical simulations of turbulent wall-bounded flows and mean cross-flow structure of rectangular ducts, Meccanica 51 (12) (2016) 3025–3042 https://doi.org/10.1007/s11012-016-0558-0.
[22] C. Chin, A.S.H. Ooi, I. Marusic, H.M. Blackburn, The influence of pipe length on turbulence statistics computed from direct numerical simulation data, Phys. Fluids 22 (2010), https://doi.org/10.1063/1.3489528.
[23] O.C. Jones, An improvement in the calculation of turbulent friction in rectangular ducts, J. Fluid Eng. 98 (2) (1976) 173–180 https://doi.org/10.1115/1.3448250.
[24] S. Gavrilakis, Numerical simulation of low-Reynolds-number turbulent flow through a straight square duct, J. Fluid Mech. 244 (1992) 101–129 https://doi.org/10.1017/S0022112092002982.
[25] A. Pinelli, M. Uhlmann, A. Sekimoto, G. Kawahara, Reynolds number dependence of mean flow structure in square duct turbulence, J. Fluid Mech. 644 (2010) 102–122 https://doi.org/10.1017/S0022112009992242.
[26] A. Huser, S. Biringen, Direct numerical simulation of turbulent flow in a square duct, J. Fluid Mech. 257 (1993) 65–95 https://doi.org/10.1017/S002211209300299X.
[27] Z. Qin, R.H. Pletcher, Large-eddy simulation of turbulent heat transfer in a square duct, Proceedings of ASME (2004) International Mechanical Engineering Congress and Exposition, Anaheim, California, Nov. 13-19 2004, Heat Transfer 1, pp. 233–246, 2004 https://doi.org/10.1115/IMECE2004-60807.
[28] K. Nishino, N. Kasagi, Turbulence statistics measurement in a two-dimensional channel flow using a three-dimensional particle tracking velocimetery, 7th Symposium on Turbulent Shear Flows, Stanford, California, 2 1989 22.1.1-22.122.1.6.
[29] M.A. Niederschulte, R.J. Adrian, T.J. Hanratty, Measurements of turbulent flow in a channel at low Reynolds numbers, Exp. Fluid 9 (4) (1990) 222–230 https://doi.org/10.1007/BF00190423.
[30] J. Kim, P. Moin, Transport of passive scalars in a turbulent channel flow, 6th Symposium on Turbulent Shear Flows, 1 1987, p. 52.
[31] H. Kong, H. Choi, J.S. Lee, Direct numerical simulation of turbulent thermal boundary layers, Phys. Fluids 12 (10) (2000) 2555–2568 https://doi.org/10.1063/1.1287912.
[32] B. Weigand, Analytical Methods for Heat Transfer and Fluid Flow Problems, Springer-Verlag Berlin Heidelberg, 2015.
[33] E.M. Sparrow, A. Garcia, W. Chuck, Numerical and experimental turbulent heat transfer results for a one-sided heated rectangular duct, Numer. Heat Tran., Part A: Applications 9 (1986) 301–322 https://doi.org/10.1080/10407788608913479.
[34] D.M. Lu, G. Hetsroni, Direct numerical simulation of a turbulent open channel flow with passive heat transfer, Int. J. Heat Mass Tran. 38 (17) (1995) 3241–3251 https://doi.org/10.1016/0017-9310(95)00048-E.
[35] N. Kasagi, A. Kuroda, M. Hirata, Numerical investigation of near-wall turbulent heat transfer taking into account the unsteady heat conduction in the solid wall, J. Heat Tran. 111 (2) (1989) 385–392 https://doi.org/10.1115/1.3250689.